

## Variations of U.S. Regional Precipitation and Simulations by the NCEP CFS: Focus on the Southwest

SONG YANG

*NOAA/Climate Prediction Center, Camp Springs, Maryland*

YUNDI JIANG

*National Climate Center, China Meteorological Administration, Beijing, China*

DAWEI ZHENG

*Shanghai Astronomical Observatory, Chinese Academy of Sciences, Shanghai, China*

R. WAYNE HIGGINS, QIN ZHANG, AND VERNON E. KOUSKY

*NOAA/Climate Prediction Center, Camp Springs, Maryland*

MIN WEN

*Chinese Academy of Meteorological Sciences, Beijing, China*

(Manuscript received 14 March 2008, in final form 31 December 2008)

### ABSTRACT

Variations of U.S. regional precipitation in both observations and free-run experiments with the NCEP Climate Forecast System (CFS) are investigated. The seasonality of precipitation over the continental United States and the time-frequency characteristics of precipitation over the Southwest (SW) are the focus. The differences in precipitation variation among different model resolutions are also analyzed.

The spatial distribution of U.S. precipitation is characterized by high values over the East and the West Coasts, especially over the Gulf Coast and southeast states, and low values elsewhere except over the SW in summer. A large annual cycle of precipitation occurs over the SW, northern plains, and the West Coast. Overall, the CFS captures the above features reasonably well, except for the SW. However, it overestimates the precipitation over the western United States, except the SW in summer, and underestimates the precipitation over the central South, except in springtime. It also overestimates (underestimates) the precipitation seasonality over the intermountain area and Gulf Coast states (SW, West Coast, and northern Midwest). The model using T126 resolution captures the observed features more realistically than at the lower T62 resolution over a large part of the United States.

The variability of observed SW precipitation is characterized by a large annual cycle, followed by a semiannual cycle, and the oscillating signals on annual, semiannual, and interannual time scales account for 41% of the total precipitation variability. However, the CFS, at both T62 and T126 resolution, fails in capturing the above feature. The variability of SW precipitation in the CFS is much less periodic. The annual oscillation of model precipitation is much weaker than that observed and it is even much weaker than the simulated semiannual oscillation. The weakly simulated annual cycle is attributed by the unrealistic precipitation simulations of all seasons, especially spring and summer. On the annual time scale, the CFS fails in simulating the relationship between the SW precipitation and the basinwide sea surface temperature (SST) and the overlying atmospheric circulation. On the semiannual time scale, the model exaggerates the response of the regional precipitation to the variations of SST and atmospheric circulation over the tropics and western Atlantic, including the Gulf of Mexico. This study also demonstrates a challenge for the next-generation CFS, at T126 resolution, to predict the variability of North American monsoon climate.

---

*Corresponding author address:* Dr. Yundi Jiang, National Climate Center, China Meteorological Administration, 46 Zhongguancun Nandajie, Beijing, 100081, China.  
E-mail: jiangyd@cma.gov.cn

## 1. Introduction

The variability of U.S. precipitation is characterized by many regional features and temporal characteristics. While the annual cycle dominates in precipitation variations over the Great Lakes, Great Plains, Midwest, Pacific Northwest, and southern California, semiannual oscillation becomes equally important over the mid-Atlantic, Southeast, and Southwest (SW) (Boyle 1998; Climate Prediction Center 2007). The semiannual oscillation is even more dominant than the annual cycle over the intermountain (IM) region. In the Northeast, the interdecadal variability of precipitation is almost as strong as the annual cycle, the most dominant time scale of the variability of the local precipitation.

The variability of precipitation is affected by both local factors (e.g., topography and soil moisture) and remote causes [e.g., the effects of sea surface temperature (SST) and large-scale natural variability] in addition to internal atmospheric processes. For example, precipitation variations are closely related to the changes in soil moisture and surface temperature (Huang and van den Dool 1993; Betts et al. 1996; Dirmeyer et al. 1999), especially over the relatively dry extratropics and during summer (Koster and Suarez 1995; Xue et al. 1996). The impact of El Niño–Southern Oscillation (ENSO) partially explains the large interannual variability of the precipitation over the southern and central-western states (Harrington et al. 1992; Hereford and Webb 1992; Higgins et al. 1998; Hu and Feng 2002; Li et al. 2005; S. Yang et al. 2007). Thus, many climate features such as droughts and floods have been attributed to the influences of oceanic and land surface processes (Namias 1983; Ropelewski and Halpert 1986; Trenberth et al. 1988; Ting and Wang 1997; Gutzler and Preston 1997; Higgins and Shi 2000; Mo and Paegle 2000; Wang and Ting 2000).

In addition to statistical relationships, climate models have also been often applied to simulate and predict precipitation variability (Betts et al. 1996; Mo et al. 2005; Saha et al. 2006; Lee et al. 2007). Although these models may not necessarily perform better than statistical tools at present, it is generally accepted that model simulation and prediction have been improved constantly during the past decades and dynamical climate prediction will become increasingly important in future climate forecast operations. The National Centers for Environmental Prediction (NCEP) Climate Forecast System (CFS) is one of the state-of-the-art global models that have been applied to understand and predict the climate of the world. As described by Saha et al. (2006), the current CFS shows important advances in operational prediction from the previous dynamical forecast efforts by demonstrating a level of prediction

skill comparable to statistical methods. Recently, Higgins et al. (2008) have compared the statistics of daily U.S. precipitation between the CFS and observations, focusing on the regional and seasonal dependence of the bias in CFS simulations in the occurrence of precipitation events, frequencies of wet and dry spells, and the changes in precipitation statistics relative to ENSO phase. The model also demonstrates skills in simulating and predicting the variability of ENSO (Wang et al. 2005) and the climate over South America (Misra and Zhang 2007), Africa (Thiaw and Mo 2005), and the Asian–Australian and Indo-Pacific sector (Wang et al. 2008; Yang et al. 2008a,b; Liang et al. 2009).

As an important component of a consolidation tool for the official forecasts of U.S. temperature and precipitation (for more information, see O’Lenic et al. 2008), the NCEP CFS not only provides information for predictions of global monsoon systems and the Madden–Julian oscillation at the NCEP Climate Prediction Center (CPC), its products are also becoming an important source of information for regional climate predictions in many countries outside the United States. For example, the CFS is one of the few operational models that participates in the annual forum on regional climate monitoring, assessment, and prediction for Asia—an activity encouraged by the World Meteorological Organization (e.g., FOCRAII 2006).

In this study, we investigate the variations of precipitation over the continental United States in both observations and the NCEP CFS. We first focus on the annual cycle of precipitation, especially its regional features because over many regions it is the most important time scale for understanding the total variations of the observed precipitation and for evaluating model performance. We then conduct a detailed analysis of the precipitation over the Southwest United States where monsoon climate prevails in summer. Here, we analyze the time–frequency characteristics of precipitation variations, using several advanced statistical analysis tools, because the variations of precipitation on different time scales are associated with different atmospheric, oceanic, and land surface conditions. We depict the differences between observations and the CFS and discuss their possible causes. Furthermore, we demonstrate the differences in precipitation simulations between low-resolution (T62) and higher-resolution (T126) versions of the CFS, which are used in the current and next-generation climate prediction operations, respectively.

## 2. Data and model simulations

The main observational data analyzed in this study include the following products: (i) the NOAA CPC

precipitation reconstruction data (PREC; Chen et al. 2002), (ii) the NCEP–National Center for Atmospheric Research (NCAR) reanalysis (Kalnay et al. 1996), and (iii) the NOAA Extended Reconstructed SST (Smith and Reynolds 2003). In particular, the PREC provides gauge-based global precipitation over lands, at a resolution of  $1^\circ$  latitude  $\times$   $1^\circ$  longitude, available from 1948 to present.

The model output is from several free-run simulations of the NCEP CFS, a coupled atmosphere–ocean–land system operational at the NCEP since August 2004 (Saha et al. 2006). The atmospheric component of the CFS is the NCEP Global Forecast System model for operational weather forecasting (Moorthi et al. 2001). It adopts a spectral triangular truncation of 62 waves (T62) in the horizontal and 64 sigma layers in the vertical with the top layer at 0.2 mb. The oceanic component is the NOAA Geophysical Fluid Dynamics Laboratory (GFDL) Modular Ocean Model version 3.0 (MOM V3) (Pacanowski and Griffies 1999), which is global longitudinally and extends from  $74^\circ\text{S}$  to  $64^\circ\text{N}$ . Its zonal resolution is  $1^\circ$ , and the meridional resolution is  $1/3^\circ$  between  $10^\circ\text{S}$  and  $10^\circ\text{N}$ , increasing gradually with latitude before becoming  $1^\circ$  poleward of  $30^\circ\text{S}$  and  $30^\circ\text{N}$ . In the vertical, the ocean model has 40 layers, with 27 layers in the upper 400 m. The vertical resolution is 10 m from the surface to the 240-m depth and increases gradually to about 511 m in the lowest layer with a bottom depth of about 4.5 km. The land surface model of the CFS is the two-layer Oregon State University model (Mahrt and Pan 1984). A new version of the operational CFS is expected to be implemented in 2010 with increased resolution (T126), improved atmospheric physics, the MOM version 4.0 (V4.0), and an improved four-layer Noah land surface model (Ek et al. 2003).

The CFS free-run simulations that were available for this analysis were made with two horizontal resolutions: T62 (about  $2^\circ$  latitude  $\times$   $2^\circ$  longitude) and T126 (about  $1^\circ$  latitude  $\times$   $1^\circ$  longitude). They include 50-yr simulations for T62 and 100-yr simulations for T126. The simulations use the initial conditions (ICs) of 1 January 2002, although ICs should play little role in long-term free runs. The atmospheric ICs are from the NCEP/Department of Energy (DOE) Global Reanalysis 2 (Kanamitsu et al. 2002), and the oceanic ICs from the Global Ocean Data Assimilation System (Behringer and Xue 2004). Except for the difference in horizontal resolutions, model physics and vertical resolutions are the same in the T62 and T126 simulations analyzed in this study. The major features of the operational NCEP CFS and the free runs have been documented by Saha et al. (2006) and Wang et al. (2005), respectively.

In our discussions, we refer to observed precipitation as PREC, and CFS precipitation as T62 and T126. Un-

less specified, we define the climatologies as the means of 57 yr (1948–2004) for PREC, 57 yr for T126, and 50 yr for T62.

### 3. Spatial patterns and annual cycles of U.S. regional precipitation

Figures 1a–e show the climatological patterns of observed precipitation for December–February (DJF), March–May (MAM), June–August (JJA), September–November (SON), and the annual mean (ANM). The precipitation patterns are generally characterized by large values in the East and small values in the West except the northwest coast in nonsummer seasons. In the East, precipitation decreases from southeast to northwest, except in JJA when relatively homogeneous precipitation appears. Heavy precipitation is mainly confined in the Gulf Coast states in SON and DJF but spreads to the Southeast in MAM and JJA (and over the Midwest in JJA). In the West, heavy precipitation occurs in a narrow, north–south oriented band over the West Coast (north of  $35^\circ\text{N}$ ), except for JJA when large precipitation appears over Mexico and the Southwest U.S. monsoon region.

The CFS T126 (Figs. 1f–j) captures many basic features of the observed precipitation, including the heavy precipitation in the East, the light precipitation in the West, and the heavy precipitation over the northwest coast in the nonsummer seasons. These features also include a tendency of southeast-to-northwest decrease of precipitation in the East. More about the differences between the observed and simulated precipitations will be discussed shortly.

The features of DJF 850-mb atmospheric circulation in the NCEP–NCAR reanalysis are characterized by westerlies to the north of  $30^\circ\text{N}$  and easterlies to the south (vectors in Fig. 2a). A ridge and a trough can be inferred over northwestern and eastern North America, respectively, and anticyclonic patterns are observed over the subtropical Atlantic and eastern Pacific correspondingly. In JJA, the westerlies are much weaker and the anticyclonic patterns expand and become more apparent (Fig. 2c). At the same time, a strong low-level jet stream is observed over the Gulf of Mexico, the southern and eastern plains, and the southern Midwest. A much weaker low-level jet stream can also be seen over the Gulf of California. A transition of the atmospheric circulation from DJF to JJA (from JJA to DJF) is evident in the pattern of MAM (SON). The above-described features can be discerned from the CFS simulations (Figs. 2f–j) as well, although discrepancies, to be discussed shortly, also exist between observations and model simulations.

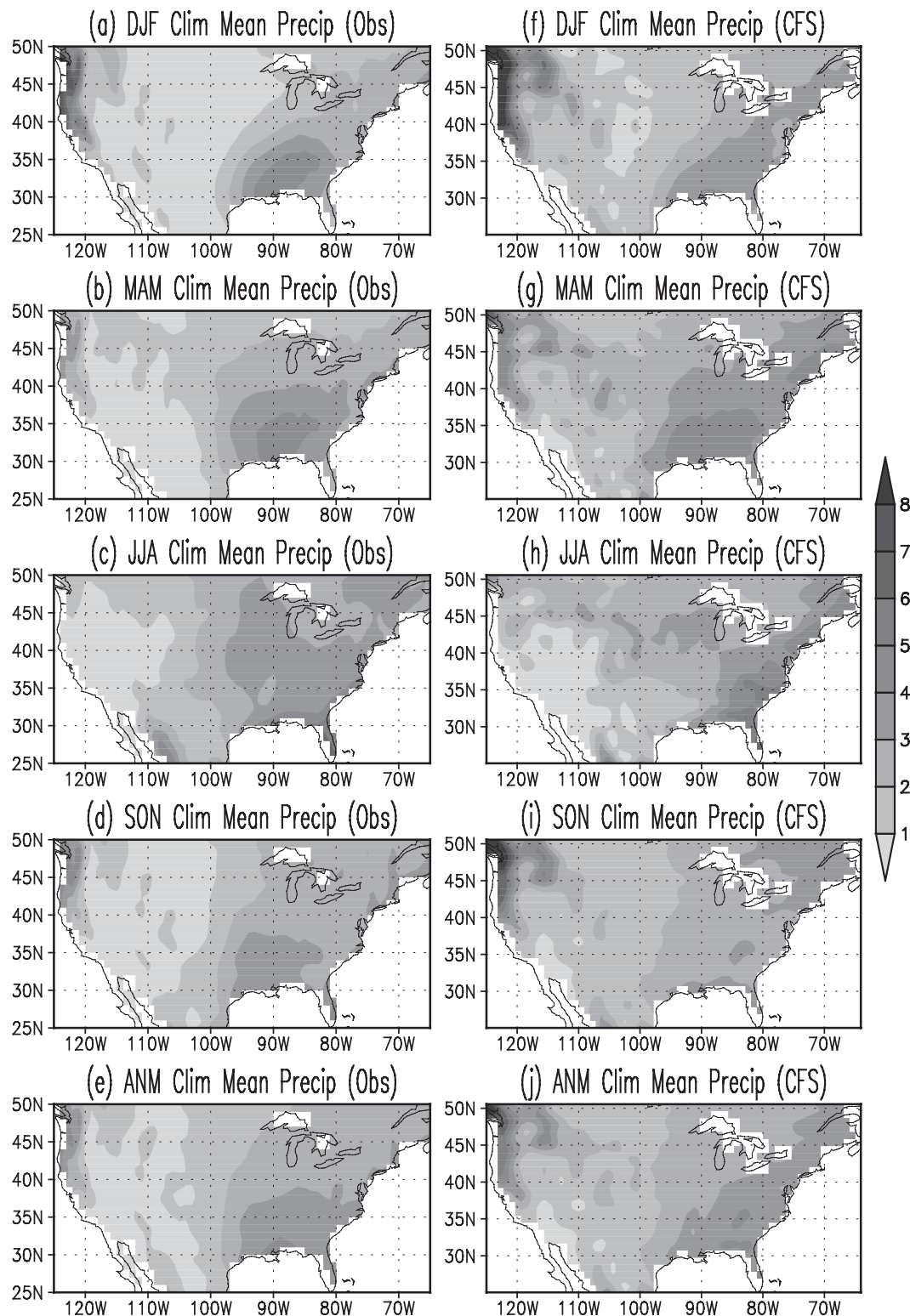


FIG. 1. (a)–(e) 1948–2004 means of observed DJF, MAM, JJA, SON, and annual precipitation (PREC) ( $\text{mm day}^{-1}$ ). (f)–(j) As in (a)–(e) but for CFS T126 precipitation of 57-yr means.

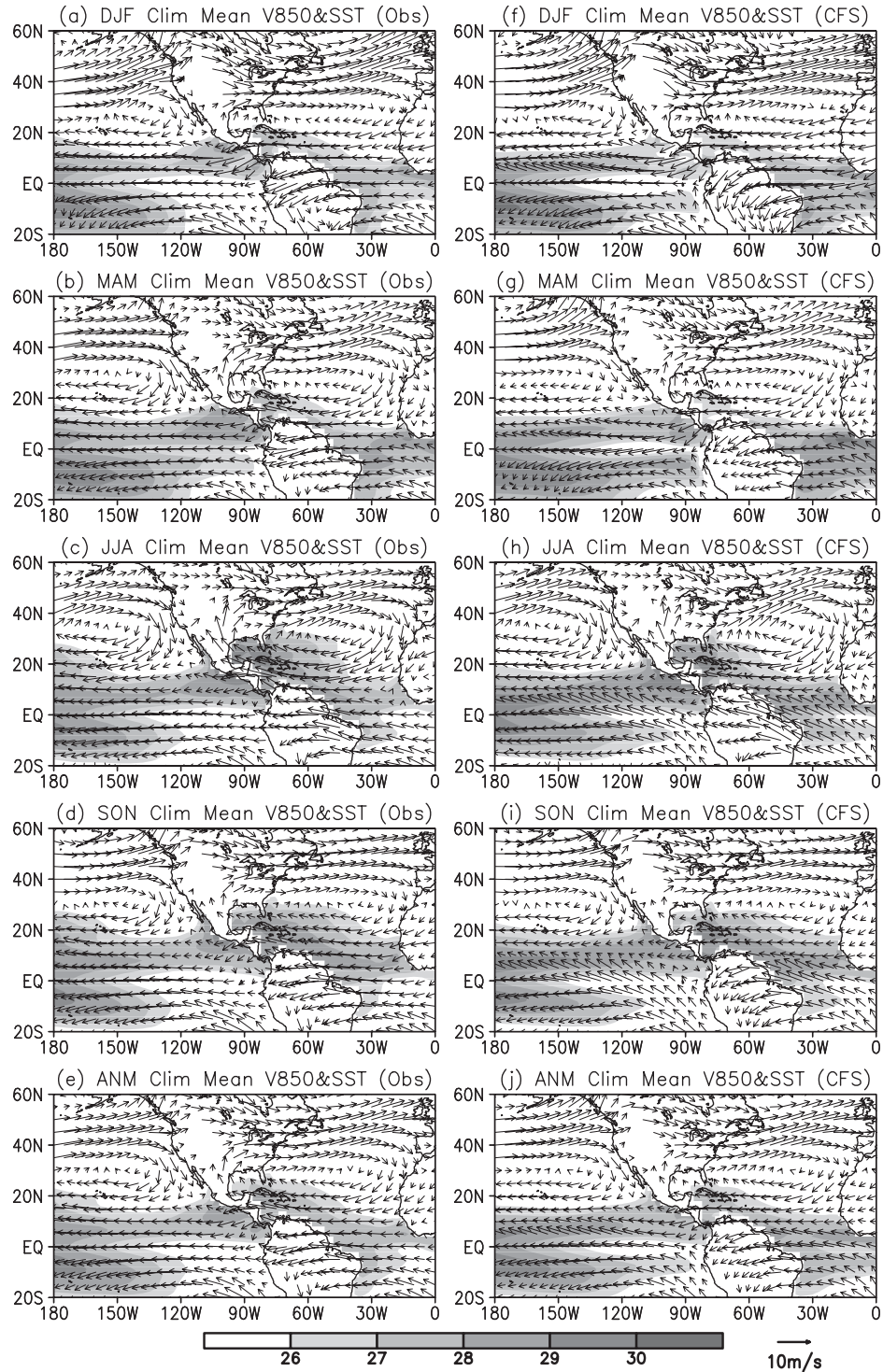


FIG. 2. As in Fig. 1 but for 850-mb winds ( $\text{m s}^{-1}$ ) (vectors) and SST ( $^{\circ}\text{C}$ ) (shading).

Figure 2 also shows that both observations and CFS simulations exhibit high SSTs over the tropical central Pacific, Atlantic, and northeastern Pacific, and low SST over the tropical southeastern Pacific (see the shadings).

Both display high SSTs over the Gulf of Mexico in JJA. The model captures the observed feature that the SST over the tropical Pacific is higher than the SST over the tropical Atlantic.

The discrepancies between CFS simulations and observations can be seen clearly from Figs. 3–4. Figures 3a–e, which show the differences in precipitation between T126 and PREC, indicate that the model overestimates the precipitation over the West, especially the Pacific Northwest, and underestimates the precipitation over the central-southern United States. In the West, the CFS precipitation is mostly larger than observed by more than  $0.5 \text{ mm day}^{-1}$ , except in JJA. In the Gulf Coast and southern Midwest states, the model precipitation is less than observed by more than  $0.5 \text{ mm day}^{-1}$  (except in MAM). The worst simulation occurs for JJA when the precipitation over the Southwest is substantially underestimated. Furthermore, a comparison of Figs. 3a–e with Figs. 3f–j indicates that T126 performs better than T62 in simulating the regional precipitation. As seen from the differences in annual means (Figs. 3e and 3j), obvious improvement from T62 to T126 occurs over the northern part of the country, especially over the northern Pacific-West (NPW) and the Great Lakes where the CFS overestimates regional precipitation. This improvement is at least partially related to the geographical effects of topography, land–water distribution, and others. Improvement can also be found in JJA and SON when the CFS underestimates the precipitation over the Gulf Coast and southern Midwest. However, the underestimation of precipitation over the Southwest has similar amplitude between T126 and T62.

Figure 4 shows the model–observation differences in 850-mb winds and SST. For T126 (left column), the model generates weaker-than-observed easterlies over the tropical Pacific around the year and unrealistic anomalous southerlies over the tropical eastern Pacific in JJA and SON. Overall, the CFS produces a weaker anticyclonic pattern over the subtropical North Pacific, associated with the anomalous southerlies over the eastern Pacific and West Coast and the excessive precipitation over the western United States. These features are also consistent with the warmer-than-observed SST over most of the eastern Pacific, especially in T62 (right column). The model also produces a weaker anticyclonic pattern over the subtropical eastern United States and Atlantic, associated with the anomalous northerlies over the eastern United States and western Atlantic, and especially the weaker-than-observed low-level jet over the Gulf of Mexico. The simulated SST over the subtropical Atlantic and the Gulf of Mexico is lower than observed. These features are consistent with the underestimated precipitation over the southeastern United States. It is also noticed that a large warm bias in the model exists over the extratropical Atlantic, especially in T62. Nevertheless, the reasons for the underestimation of subtropical highs, which is perhaps a

fundamental problem for climate modeling, cannot be easily understood. The errors shown in Fig. 4 are systematic and tend to form recognizable flows in which the SST patterns look consistent. Simulations in the Hadley cell-type forcing and near-equatorial convection, in addition to SST, should be further analyzed. More about the model–observation differences in atmospheric circulation and SST patterns associated with the SW precipitation will be discussed in the next section.

Since the annual cycle is the most dominant oscillating time scale of precipitation variability over many U.S. regions and it presumably yields useful information for understanding the total variations of precipitation, we conduct a more detailed analysis of the annual cycle of precipitation by applying the seasonality index defined by Walsh and Lawler (1981), which measures the magnitude of seasonality of local precipitation (also see Li et al. 2005). The seasonality index is defined as

$$\text{SI} = \frac{1}{\bar{P}} \sum_{m=1}^{12} \left| P_m - \frac{\bar{P}}{12} \right|, \quad (1)$$

where  $\bar{P}$  is the total precipitation of a given year, and  $P_m$  is the precipitation for month  $m$ . That is, the value of the index in a given year measures the sum of the absolute deviations of monthly precipitation from the overall mean, divided by the total annual precipitation of the year. A high (low) value of the index measures a large (small) annual cycle of the precipitation over a specific region. However, the value alone does not provide any information about the phase of the annual cycle. Therefore, although the index is useful for depicting the amplitude of precipitation annual cycles over a spatial pattern conveniently, it should be combined with other analyses to reveal the detailed features of the annual cycle of regional precipitation (see Fig. 7).

Figure 5a shows large seasonality of the observed precipitation over the Southwest, the West Coast, and the Great Plains and small seasonality over the East except in Florida. The intermountain region is a low-value area, surrounded by large values of precipitation seasonality. The CFS T126 produces large precipitation seasonality over the West Coast and the central Great Plains and small seasonality over the eastern third of the country (Fig. 5b). These features are in general agreement with the observed features shown in Fig. 5a. However, discrepancies between Fig. 5 and Fig. 5b are also apparent and these discrepancies can be more clearly identified from Fig. 6a, which depicts the differences in precipitation seasonality between observations and CFS T126. Large differences are found over the U.S. Southwest/northern Mexico where the differences (Fig. 6a) are even larger than the values of simulated seasonality (Fig. 5b). Another

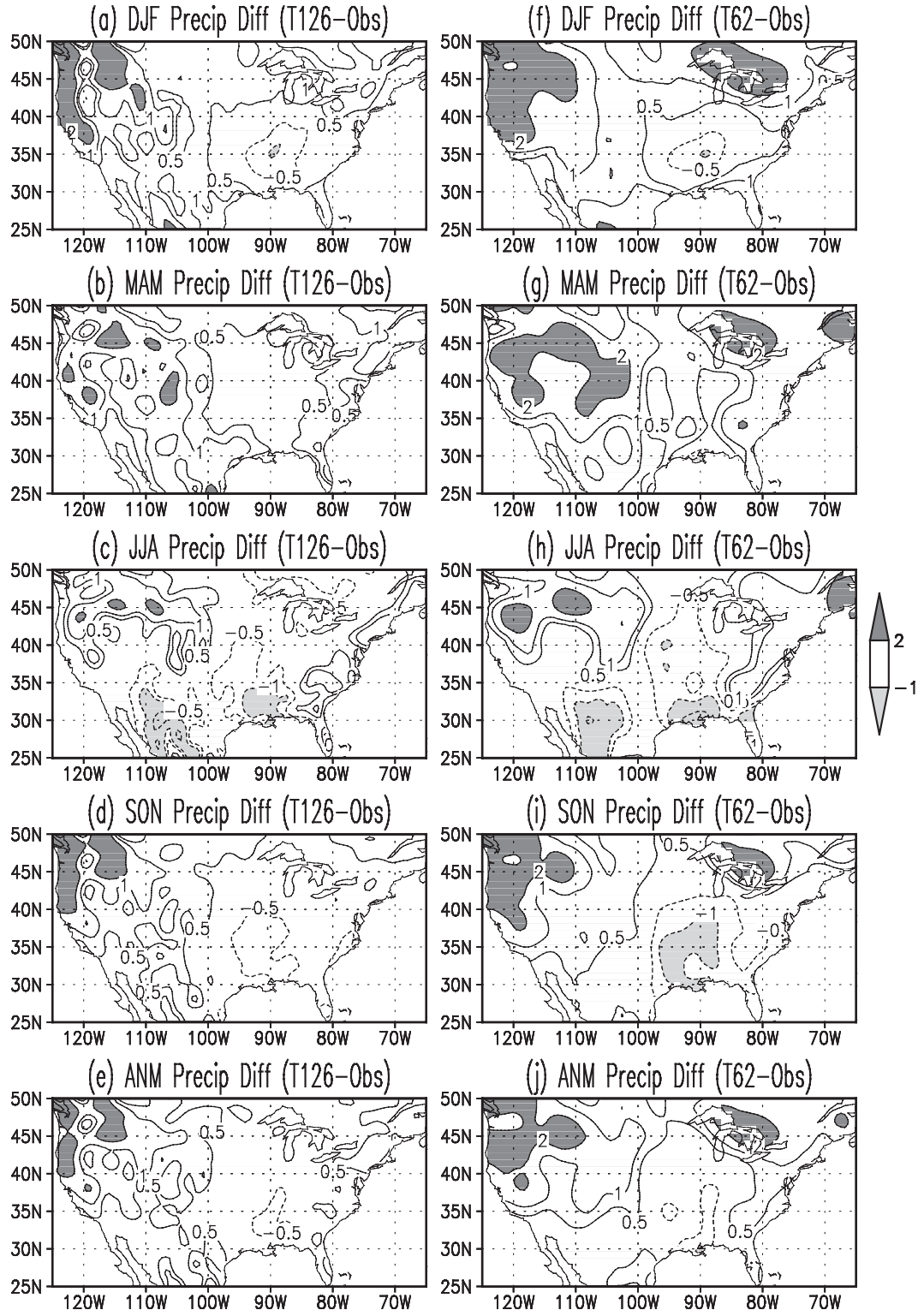


FIG. 3. (a)–(e) Differences in DJF, MAM, JJA, SON, and annual climatological precipitation ( $\text{mm day}^{-1}$ ) between CFS T126 and PREC. (f)–(j) As in (a)–(e) but between CFS T62 and observations.

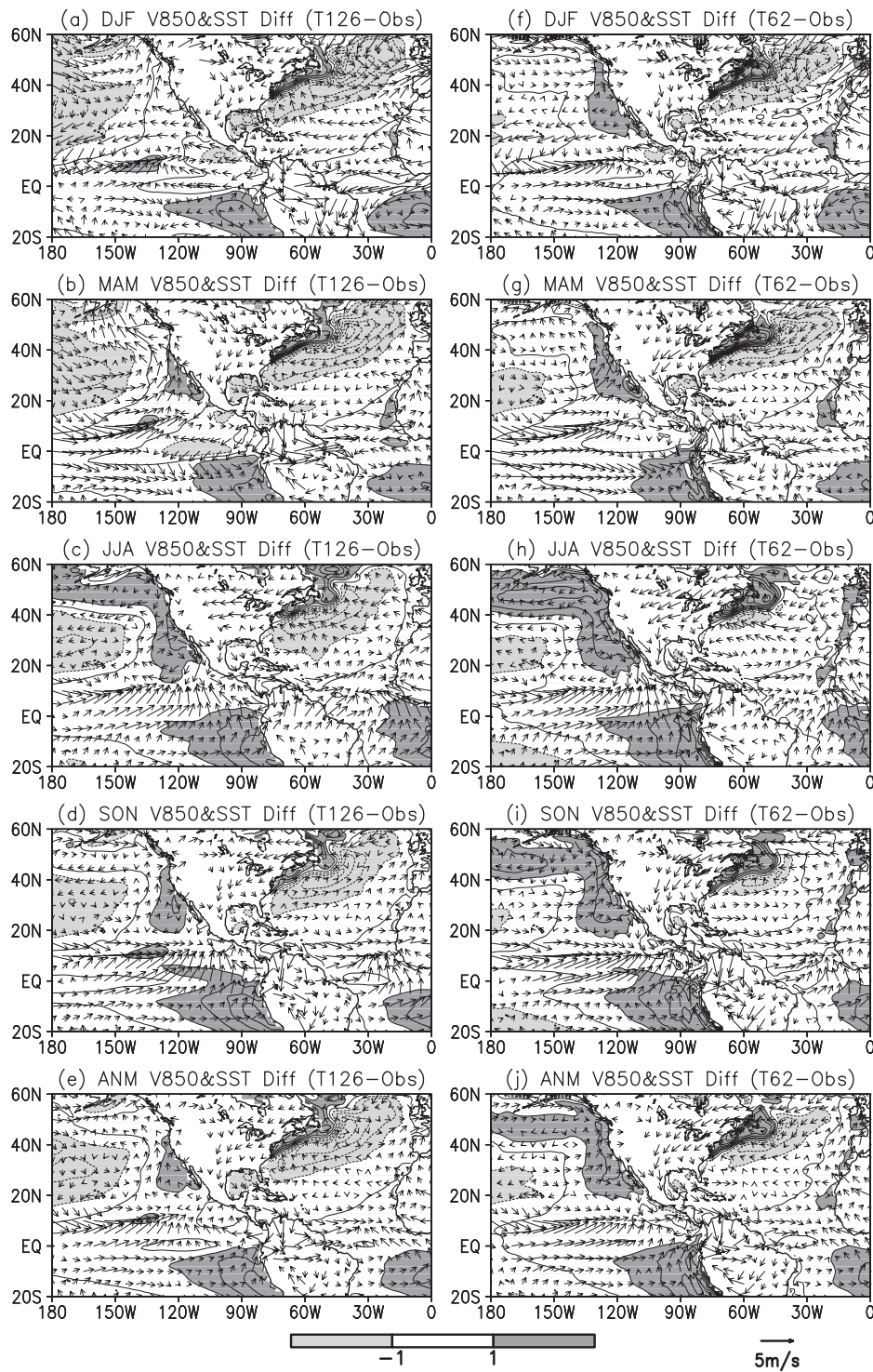


FIG. 4. As in Fig. 3 but for 850-mb winds ( $\text{m s}^{-1}$ ) (vectors) and SST ( $^{\circ}\text{C}$ ) (contours in interval of 1 and shadings).

area of large differences is the intermountain region where the model overestimates the precipitation seasonality. On the other hand, smaller model – observation differences are found over the eastern half of the country. A com-

parison of Figs. 6a with 6b reveals only small differences with changes in model resolution, with a slight improvement in model simulations of precipitation seasonality from T62 to T126 over the Gulf Coast states and the

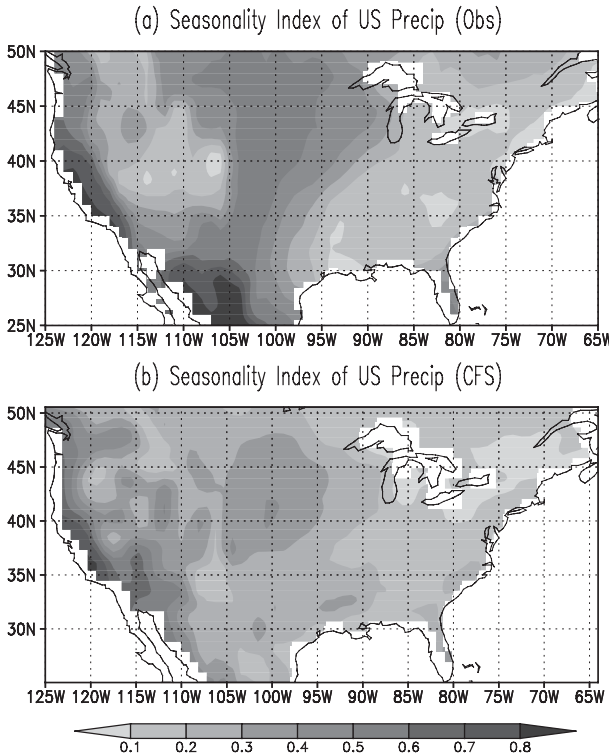


FIG. 5. Precipitation seasonality for (a) PREC and (b) CFS T126.

intermountain region. However, little or no improvement is evident over the U.S. Southwest/northern Mexico.

The detailed features of precipitation seasonal cycles are investigated by examining the monthly climatological precipitations averaged over particular spatial domains. We select these domains based on the difference values of precipitation seasonality between observations and T126 simulations. As shown in Fig. 6a, we focus on the NPW, southern Pacific West (SPW), SW, and central north (CN), where the CFS produces smaller-than-observed precipitation seasonality. We also focus on the IM and central south (CS), where the CFS overestimates precipitation seasonality and the northern East Coast (NEC) and southern East Coast (SEC) where the CFS well simulates the precipitation seasonality. In the figure, the dashed box near SW delineates the North American Monsoon Experiment (NAME) tier-1 domain ( $20^{\circ}$ – $35^{\circ}$ N,  $115^{\circ}$ – $105^{\circ}$ W) for which the variability of precipitation will be analyzed later.

In NPW (Fig. 7a), the observed precipitation reaches a maximum in DJF and minimum in July, followed by August. The CFS simulations yield similar annual cycles in which precipitation is minimum in August and maximum in November–January. However, the model exhibits a significant wet bias, although it is smaller in T126 than in T62. The CFS also simulates the seasonal cycle of

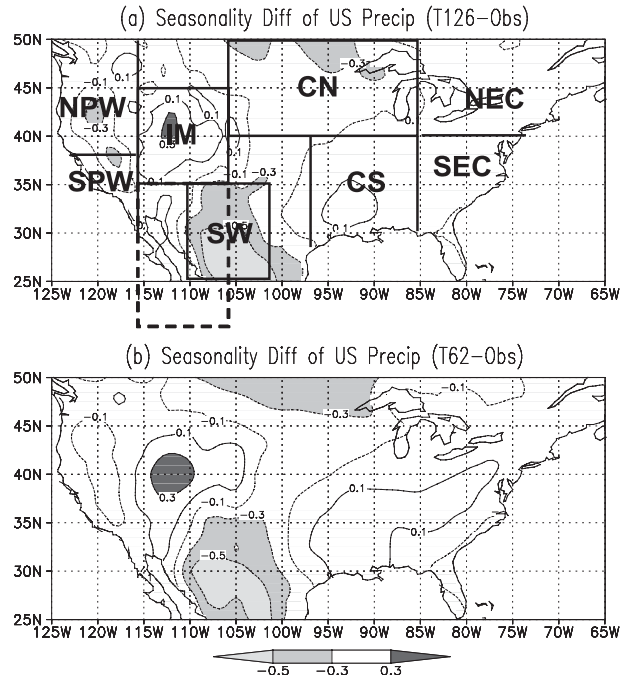


FIG. 6. Differences in precipitation seasonality (a) between CFS T126 and PREC and (b) between CFS T62 and PREC. The solid boxes outline domains of northern Pacific West (NPW), southern Pacific West (SPW), intermountains (IM), Southwest (SW), central north (CN), central south (CS), northern East Coast (NEC), and southern East Coast (SEC). The dashed box in the southwest outlines the NAME tier-1 domain.

precipitation over the SPW quite well (Fig. 7b). It captures the precipitation in JJA realistically. However, the model also exhibits a wet bias during the nonsummer months, especially in T62. In the IM (Fig. 7c), where the observed precipitation reaches maximum in May and minimum in winter and has the smallest annual cycle compared to other domains, both T62 and T126 overestimate the precipitation significantly, especially T62. The model also significantly exaggerates the annual cycle of precipitation. Here, the climate of the coasts is pushed into the Great Basin, but the coarse CFS does not have enough topographical forcing to block the flow.

The worst CFS simulations of the annual cycle of precipitation occur in the SW (Fig. 7d). Here, the observed precipitation is maximum in July and minimum in March. However, the maximum of T62 precipitation appears in February and the minimum in June. T126 attains a maximum in September and a secondary maximum in March and two minima in January and July, respectively, yielding an apparent semiannual cycle. This problem in simulating SW precipitation by the CFS will be further diagnosed in the next section.

In CN (Fig. 7e), the CFS realistically simulates the monthly climatological precipitation during summer and

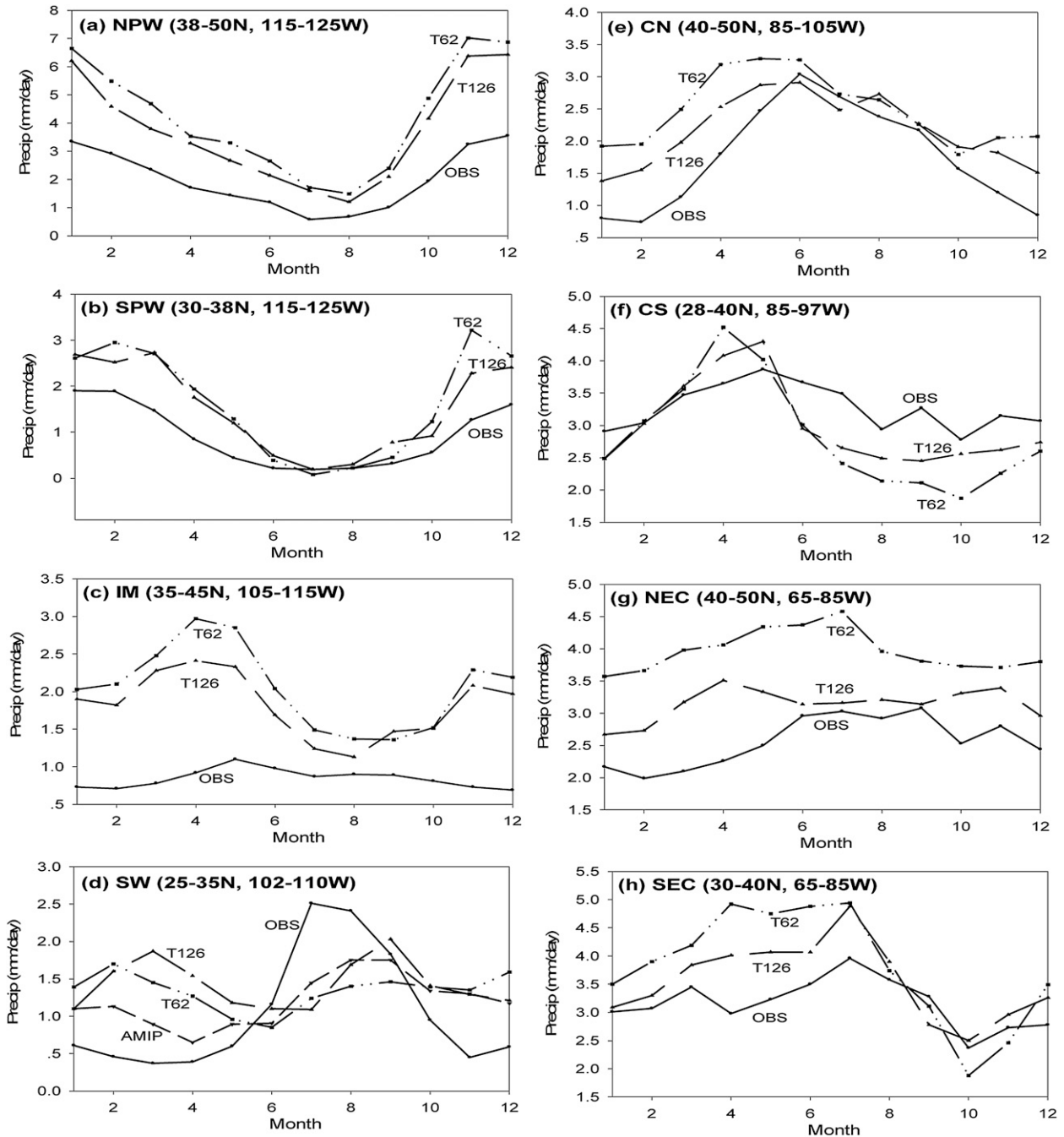


FIG. 7. Area averages of monthly climatological precipitation ( $\text{mm day}^{-1}$ ) in (a) PREC, (b) CFS T62, and (c) CFS T126 over different domains outlined in Fig. 6a. Result from an AMIP experiment (1949–2004) is also shown in (d) for later discussion.

fall months. However, it overestimates the winter and spring precipitation, especially T62. The CFS exaggerates the annual cycle of precipitation over CS (Fig. 7f), with the maximum (minimum) precipitations in spring (fall) being greater (less) than observed. In NEC where precipitation seasonality is among the smallest (Fig. 7g), the CFS captures the seasonal cycle of the observed

precipitation reasonably well. However, the model (especially T62) significantly overestimates the precipitation, although T126 simulates the precipitation during June–September realistically. This region contains modest topographical relief but includes the Great Lakes. The improvement from T62 to T126 suggests the importance of the influence of land and lake surface

processes in the CFS. In SEC (Fig. 7h), the maximum (minimum) precipitation occurs in July (October) in both observations and the CFS. The model captures the seasonal cycle reasonably well. However, while the CFS simulates the precipitation during August–December quite realistically, it overestimates the regional precipitation during the other months, especially by the T62.

In short, the CFS improves the simulations of the U.S. regional precipitation overall, especially over the Pacific West and the Great Lakes regions, when its resolution increases from T62 to T126. However, over the Southwest, where the largest annual cycle of observed precipitation exists, the CFS has considerable difficulty in simulating the variability of the precipitation, and the increase in model resolution does not improve precipitation simulations. In the next section, we further carry out an analysis of the variability of SW precipitation, focusing on the detailed features of its time–frequency characteristics and the physical processes associated with the weak annual cycle shown above. For CFS output, we focus on the simulation by the T126.

#### 4. Analysis of the variations of Southwest precipitation

We first apply wavelet transform (Morlet et al. 1982) and least squares analyses to reveal the time–frequency characteristics of the SW precipitation. As in S. Yang et al. (2007), we apply a leap-step time series analysis (LSTSA) (Zheng et al. 2000) to improve the data information of the end points in the wavelet analysis. The LSTSA is a nonlinear model that decomposes a time series into deterministic and stochastic components. The stochastic component is further characterized by several stochastic models, each of which is valid within a subdomain of the time series. The analysis effectively reduces the edge effects of the filtered output signals and provides a better stability for long-range forecasts.

Figure 8a shows that the annual cycle of the observed precipitation is predominantly strong, although it becomes weaker after 2000. The semiannual signal also has large amplitude but it is secondary to the annual oscillation and relatively unstable in time. Since the 1970s, a quasi-biennial signal is evident as well. The largest difference between the observed and CFS spectrum occurs in the amplitude of the annual cycle, which decreases substantially in the model simulations (see Fig. 8b).

We further quantitatively determine the mean magnitudes and phases of the temporal variations of the SW precipitation by applying a least squares method, focusing on the features of five time scales (semiannual, annual, quasi biennial, interannual, and interdecadal)

with strongest signals. The least squares method of the Householder transform (Powell and Reid 1969), which is a linear regression problem, is given as follows:

$$SL_t = a + bt + \sum_{k=1}^5 c_k \sin(2\pi t/P_k + \varphi_k) + \varepsilon_t, \quad (2)$$

where  $P_k$ ,  $c_k$ , and  $\varphi_k$  are, respectively, the periods, amplitudes, and phases of the aforementioned oscillating terms and  $a$  and  $b$  are the constant and linear terms. Since the periods of interannual and interdecadal fluctuations are relatively unstable and drifts in frequency may occur in the spectral estimate (see Fig. 8), we determine their mean values by a method of trial and error in the process of least squares computations. Specifically, we identify and determine the optimal mean periods of the spectral signals by adjusting the periodic values step by step. In this process, the amplitudes and phases of the spectral signals are also estimated and the uncertainties in period of the signals are measured by the standard deviations of phases.

Table 1 shows that the annual and semiannual variations of the observed precipitation have the largest amplitudes (0.91 and 0.53 mm day<sup>-1</sup>, respectively) and the most stable phases [measured by the smallest rms value (0.01) presented in the third column]. The SW precipitation also fluctuates relatively stably on the quasi-biennial time scale. In the CFS, the largest amplitude appears at the semiannual time scale (0.4), and the annual signal is unrealistically small (0.14). Indeed, the simulated annual signal has only about 15.4% of the observed signal and is only 35% of the simulated semiannual signal. Another apparent discrepancy in Table 1 is that, on the interannual time scale (3.27 yr for PREC and 3.69 yr for the CFS), the simulated amplitude is twice as large as observed. Table 1 also shows increasing trends of the SW precipitation, 0.1 mm day<sup>-1</sup> century<sup>-1</sup> for both observation and the CFS.

The rms value of 0.54 mm for PREC is calculated from the residual series after the five oscillating signals shown in Table 1 and the constant and linear trend terms are removed from the observed monthly precipitation data. The contribution of the oscillating signals to the rms of monthly SW precipitation (0.921 mm) is 41% [i.e.,  $(0.921 - 0.54)/0.921$ ], resulted largely from annual and semiannual time scales. However, in the CFS, the RMS value is so large (0.794 mm) that the oscillating signals only contribute 7% [ $(0.855 - 0.794)/0.855$ ] to the rms of monthly SW precipitation (0.855 mm), with the largest contribution from the semiannual time scale instead of the annual time scale. This result indicates that the variations of SW precipitation are significantly less oscillating in the CFS than in observations.

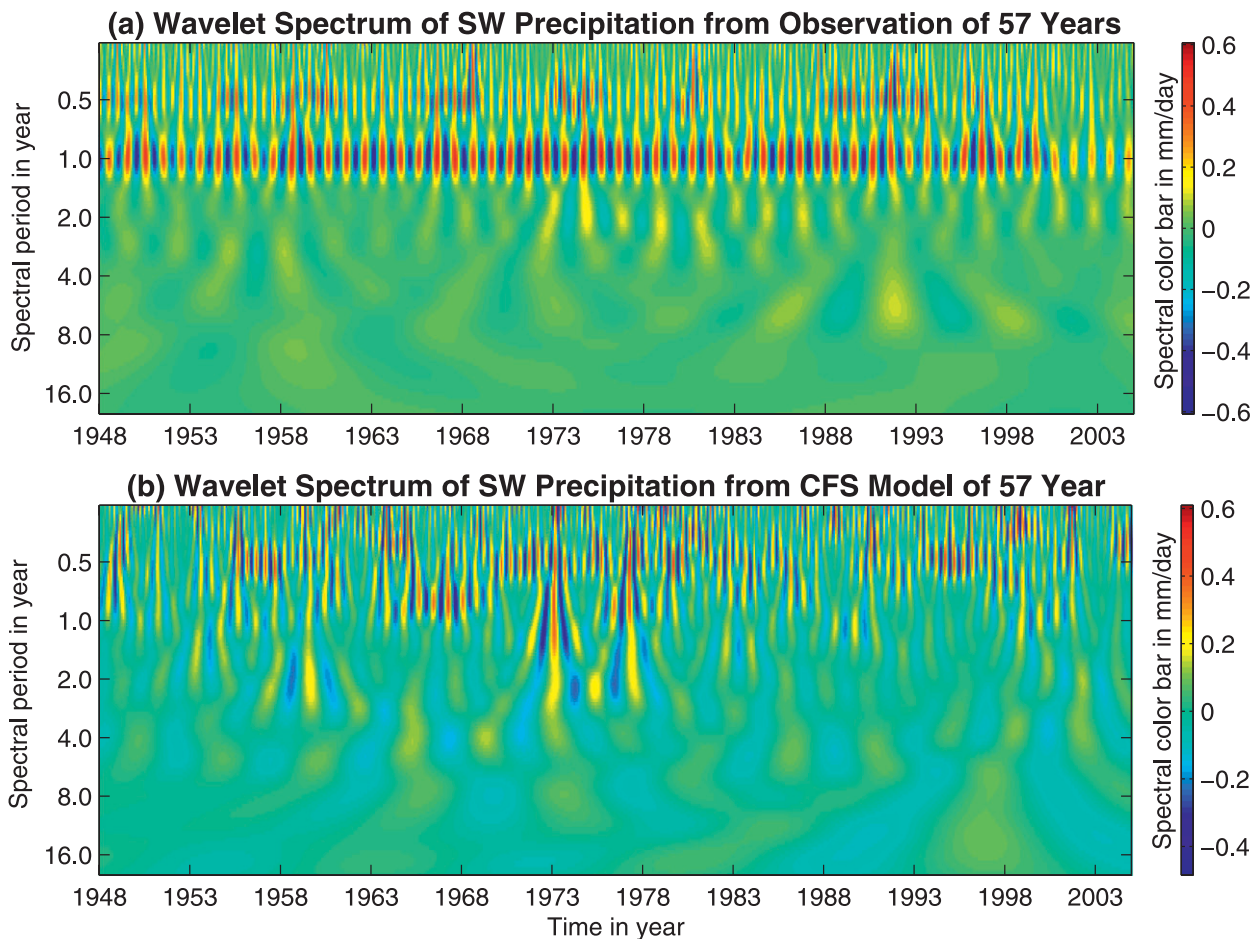


FIG. 8. Wavelet time–frequency spectrum of monthly SW precipitation ( $\text{mm day}^{-1}$ ) for (a) PREC and (b) CFS. The years for the CFS are arbitrary.

A more thorough estimation of the amplitude and phase of the signals from successive subseries with 1-yr span reveals several important features: 1) The mean difference (observation minus CFS) in the amplitude series is  $0.66 \text{ mm day}^{-1}$  for the annual signal. 2) The mean difference in the phase series is  $81.3^\circ$  (lag by about 2 months) for the semiannual signal. That is, in the

model SW precipitation, a bias of small amplitude of the annual cycle (always smaller than observed) and a bias of phase lag of the semiannual signal exists. Thus, it is important for improving the simulation of precipitation if the model annual cycle is enhanced and the error in the phase of model semiannual signal is corrected, although this is a challenging task.

TABLE 1. Parameter estimations of five most apparent signals calculated from observed and CFS monthly SW precipitation.

PREC			CFS		
Period (yr)	Amplitude ( $\text{mm day}^{-1}$ )	Phase (yr)	Period (yr)	Amplitude ( $\text{mm day}^{-1}$ )	Phase (yr)
0.50	$0.53 \pm 0.03$	$0.07 \pm 0.01$	0.50	$0.40 \pm 0.04$	$-0.01 \pm 0.01$
1.00	$0.91 \pm 0.03$	$-0.32 \pm 0.01$	1.03	$0.14 \pm 0.04$	$-0.10 \pm 0.05$
2.01	$0.10 \pm 0.03$	$-0.06 \pm 0.09$	2.04	$0.14 \pm 0.04$	$-0.65 \pm 0.10$
3.27	$0.06 \pm 0.03$	$-0.14 \pm 0.24$	3.69	$0.13 \pm 0.04$	$-1.62 \pm 0.20$
12.05	$0.09 \pm 0.03$	$3.72 \pm 0.65$	10.92	$0.12 \pm 0.04$	$-2.26 \pm 0.61$

Linear rate:  $0.001 \pm 0.001 \text{ mm day}^{-1} \text{ yr}^{-1}$   
Rms: 0.540 (0.921, 41%)

Linear rate:  $0.001 \pm 0.002 \text{ mm day}^{-1} \text{ yr}^{-1}$   
Rms: 0.792 (0.855, 7%)

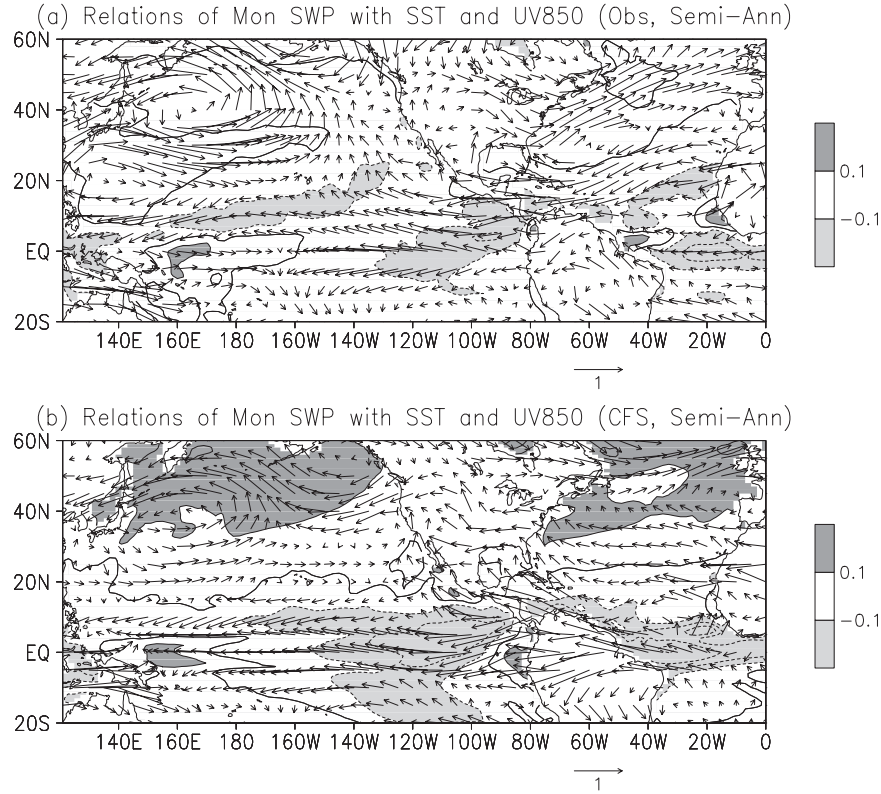


FIG. 9. Correlations between grid-SST and the semiannual signals of the SW precipitation (contours in interval of 0.1 and shadings) and regressions of 850-mb winds against the semiannual signals of the precipitation (vectors:  $\text{m s}^{-1}$ ). Results are shown for (a) observations and (b) the CFS.

To display the oscillating signals of SW precipitation variability more clearly, as in S. Yang et al. (2007), we apply a multistage filter (MSF) (Zheng and Dong 1986) to extract these signals in different frequency bands: semiannual (5–7 months), annual (10–13 months), quasi biennial (20–28 months), and interannual (2.5–6.7 yr). (We also apply the LSTSA model described above in the filtering process to reduce the edge effect of the filtered signals.) In choosing the time windows for the various frequency bands, we not only allow the signals to be passed as completely as possible, but also avoid the overlapped effects of the signals on the truncated bands. Additionally, we consider the features of precipitation variations from the wavelet estimate discussed above. Thus, while narrower bands are chosen for the annual and semiannual time scales, wider bands are chosen for the relatively unstable quasi-biennial and interannual signals. As shown in Table 1, the MSF analysis also indicates that the SW precipitation most strongly oscillates on the annual and higher time scales. The amplitude of the quasi-biennial and interannual signals is small and is comparable between the two time scales. The CFS underestimates the annual signal of the

SW precipitation variations but overestimates the signals over the lower frequency bands. The model annual and semiannual signals are also less stable than observed. On the interannual time scale, the model signal is more stable than the observed signal, and the model precipitation is more significantly correlated to the Niño-3.4 SST than is the observed precipitation.

Figure 9a presents the observed features of the correlations of grid SST with the semiannual signal of the SW precipitation and the regressions of 850-mb winds against the precipitation signal. On the semiannual time scale, an increase in the observed SW precipitation is associated with enhanced easterly trade winds and generally cooling conditions (except 150°E–160°W) over the tropics. It is also associated with a cyclonic pattern and weak cooling over the western-central North Pacific and an anticyclonic pattern and weak warming over the North Atlantic, in the extratropics. The Atlantic anticyclonic pattern also extends to the Gulf of Mexico and provides water vapor supply to Mexico and the southwestern United States. The CFS produces very similar large-scale features for this particular time scale (Fig. 9b). Intensification of the trade winds and cooling conditions

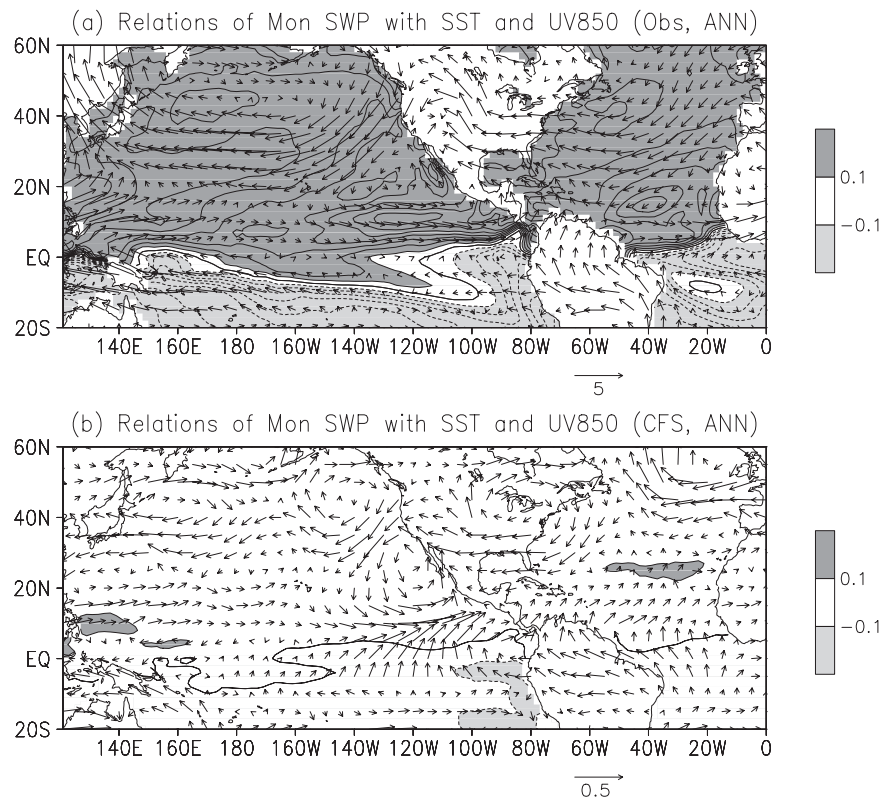


FIG. 10. Correlations between grid-SST and the annual signals of SW precipitation (contours in interval of 0.1 and shadings) and regressions of 850-mb winds against the annual signals of the precipitation (vectors:  $\text{m s}^{-1}$ ). Results are shown for (a) observations and (b) CFS.

associated with an increase in SW precipitation appear clearly over the tropics (except the equatorial western Pacific). The U.S. southwest and Mexico also receive water vapor from the Gulf of Mexico and the Caribbean Sea, although the water supply is larger than observed. In the extratropics and subtropics, a cyclonic pattern is seen over the North Pacific and an anticyclonic pattern lies over the North Atlantic, as in the observations.

However, the relationship between weakening westerlies and warming SST over the extratropical Pacific and the connection between the anticyclonic pattern and warming SST over the extratropical Atlantic are both stronger in the CFS than in observations. The more serious problem found between Figs. 9a and 9b is the circulation pattern over the United States. In observations, increasing SW precipitation is associated with anomalous westerlies over the Southeast and north of  $40^{\circ}\text{N}$ . However, anomalous easterlies cover the entire United States in connection with increasing SW precipitation in the CFS. The exaggerated SST–precipitation correlations over the tropical eastern Pacific and Atlantic suggest that the SW precipitation overly responds to the regional SSTs on the semiannual time scales. Since the model SST over the tropical eastern

Pacific is too cold in winter but too warm in summer (see Fig. 4), this exaggerated negative relationship implies that the model precipitation is above (below) that observed in winter (summer), as seen from Fig. 7. Figure 9 also shows that in the CFS the SW precipitation is more strongly related to the flow from the Gulf of Mexico; however, the jet stream over the gulf is too weak in the model.

Figure 10a shows the observed relationships of grid SST and 850-mb winds with the annual signals of SW precipitation. The annual oscillation of the precipitation is embedded in a clear annual change in thermal conditions on a global scale. That is, the maximum SW precipitation in July–September (see Fig. 7d) is involved with warming in the Northern Hemisphere and cooling in the Southern Hemisphere, and the minimum precipitation in winter and early spring is associated with cooling in the Northern Hemisphere and warming in the Southern Hemisphere. Regionally, the annual precipitation signals are most strongly correlated with the SSTs over the tropical northeastern Pacific, the Gulf of Mexico, and subtropical northwestern Atlantic and Pacific. Figure 10a also shows that, as the SW precipitation increases from winter–spring to summer (see Fig. 7d),

the Northern Hemisphere westerlies become weaker and the atmospheric circulation over the North Pacific and from the eastern United States to the Atlantic grows to be more anticyclonic. Perhaps the more important features of the figure are the enhanced cyclonic pattern over the tropical–subtropical northeastern Pacific and southwestern United States and the large water vapor transport from the Gulf of Mexico and the Caribbean Sea, associated with the increase in SW precipitation. The latter feature reflects the relationship between the monsoon systems over North and South America on their annual transition.

In the CFS (Fig. 10b), the annual signal of SW precipitation is associated with very different physical processes from that observed. First of all, the relationships of precipitation with SST and atmospheric circulation on the annual time scale are much weaker in the model. Although the CFS precipitation–SST correlation is also positive in the Northern Hemisphere and negative in the Southern Hemisphere, the relationship, especially that over the eastern Pacific warm pool and the Gulf of Mexico, is tremendously small and insignificant. Figure 10b shows a number of features that can be observed from Fig. 10a, which include the anomalous cyclonic patterns over the northern extratropics, the weakening of subtropical westerlies and tropical trade winds associated with an increase in SW precipitation, and the anomalous cyclonic pattern over the subtropical northeastern Pacific. However, these features, including the atmospheric circulation over the Gulf of Mexico which is in general associated with the broader-scale subtropical high and the local SST, are about 10 times smaller than that observed. The weak relationships of the model precipitation with the SST and winds over the entire analysis domain suggest a lack of the link of SW precipitation to the basinwide SST from the CFS on the annual time scale. We repeat the computation for Fig. 10 and obtain a pattern similar to that shown in Fig. 10a if observed SW precipitation and modeled winds and SST are used. However, we obtain a pattern similar to that shown in Fig. 10b if modeled SW precipitation and observed winds and SST are used. This analysis further suggests the potential effects of large-scale atmospheric circulation and SST patterns on the SW precipitation.

The above discussions of the importance of SST anomalies over the tropical eastern Pacific and the Gulf of Mexico are in agreement with the findings of previous studies. For example, the precipitation over central-northern America varies with the lagged feedbacks between the SST over the tropical eastern Pacific warm pool, local convection, and surface insulation (Magaña et al. 1999). The precipitation is also affected by the subtropical western Atlantic high (Hastenrath 1967),

which links to the change in SST over the Gulf of Mexico. A brief examination of the output from Atmospheric Model Intercomparison Project (AMIP) experiments (forced by observed SST) with an earlier version of the atmospheric model of the CFS (T62) also indicates the importance of SST for realistic simulation of the SW precipitation. It can be seen from Fig. 7d that, compared with precipitation in the free run, the AMIP precipitation is smaller during December–April and larger during July–September. Thus, the mean annual cycle of the AMIP precipitation is more similar to that observed, compared to the annual cycle in the free run. More results about the AMIP experiments using similar atmospheric models of the CFS can be found in Mo et al. (2005).

We further analyze features of vertically integrated water vapor transport, which are closely linked to the features of atmospheric circulation and precipitation. We analyze monthly values because they can depict the features on both annual and semiannual time scales and illustrate the seasonality of water vapor transport. Figure 11 shows that, in observations, water vapor is transported to the SW domain from the western boundary (except in July–August) and from the southern boundary (except in June). More water vapor crosses the west than from the south, except in September. Water vapor exits the domain from the north (except November–February) and from the east (except July–September). Relatively, more water vapor leaves the SW from the north during June–September and from the east during October–May. In other words, from November to February, water vapor exits the SW from the east and enters the domain from all other boundaries. During July–September, however, water vapor enters the SW from the east and the south and exits the domain from the north and the west. Figure 11 also shows a convergence of water vapor flux during June–October and a divergence in the other months. The largest water vapor convergence occurs in July–September when the area-averaged precipitation is high, while the largest divergence is observed in April when the area-averaged precipitation is among the lowest.

Figure 12 shows that the CFS captures several main features observed in water vapor transport. For example, except in July–September, the directions of water vapor flux across the various boundaries of the SW domain in the model are identical to those in the observations. As observed, the water vapor fluxes over the western and eastern boundaries are often larger than those over the southern and northern boundaries (except June–September), and the net water vapor transport is mostly negative.

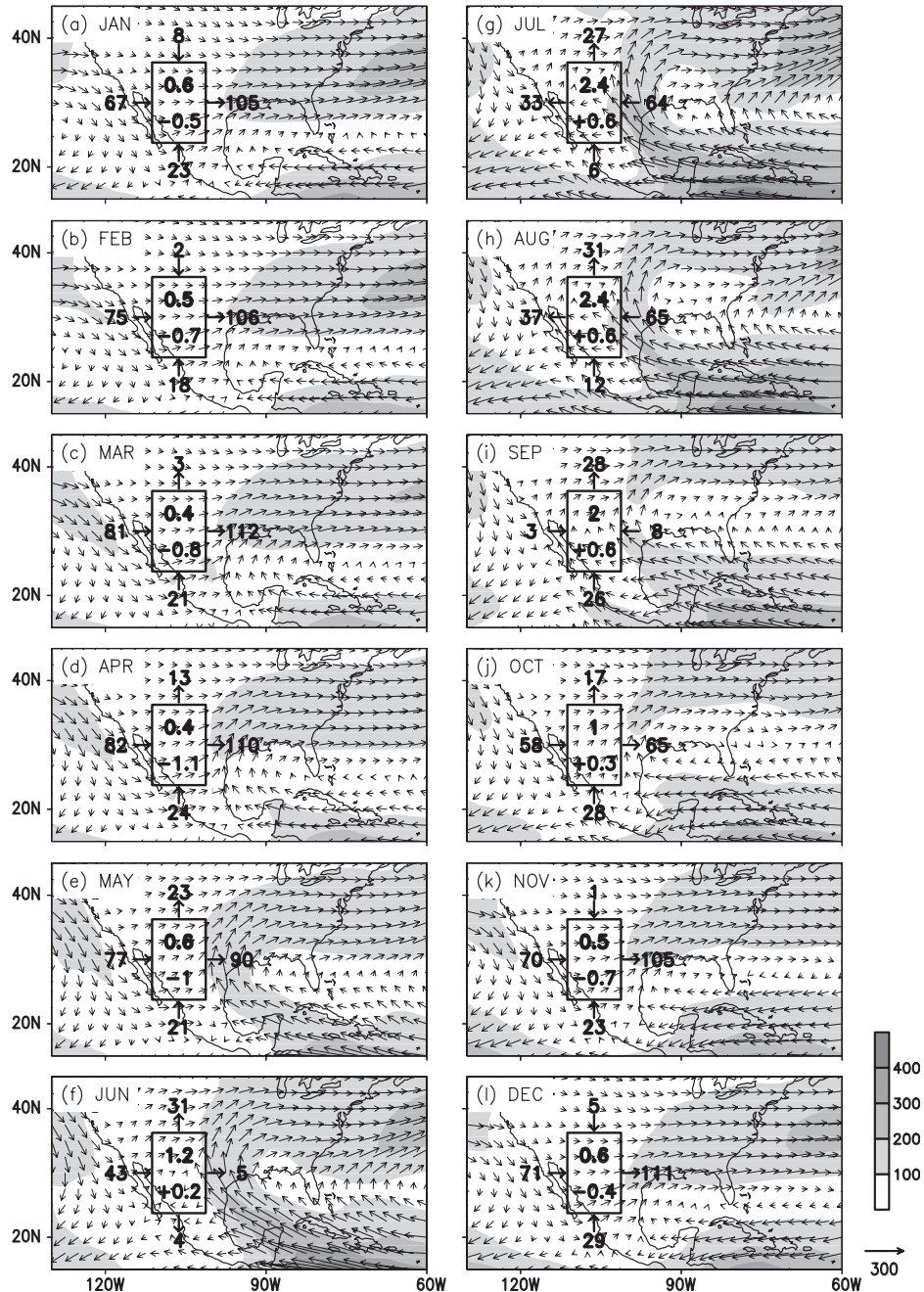


FIG. 11. Monthly climatologies of vertically integrated water vapor flux (vectors:  $\text{kg m}^{-1} \text{s}^{-1}$ ) and its magnitude (shadings) from the NCEP-NCAR reanalysis. Numbers outside the boxes over the SW domain illustrate the total water vapor fluxes across the boundaries ( $10^6 \text{ kg s}^{-1}$ ) and the arrows indicate the directions of these fluxes. The respective top and bottom numbers inside the boxes denote the average precipitation ( $\text{mm day}^{-1}$ ) and the net values of water vapor flux ( $\text{mm day}^{-1}$ ) over the domain.

However, comparison between Figs. 11 and 12 also indicates major discrepancies between the CFS and observations. First, for June and August, the net water vapor transport is positive in observations but negative in the CFS, which partially accounts for the deficit in

model precipitation in these months. Second, in the CFS, a smaller loss of water vapor occurs in late winter and spring, associated with an unrealistically large amount of precipitation. This small loss of modeled water vapor, which contributes to the exaggerated semianual signal,

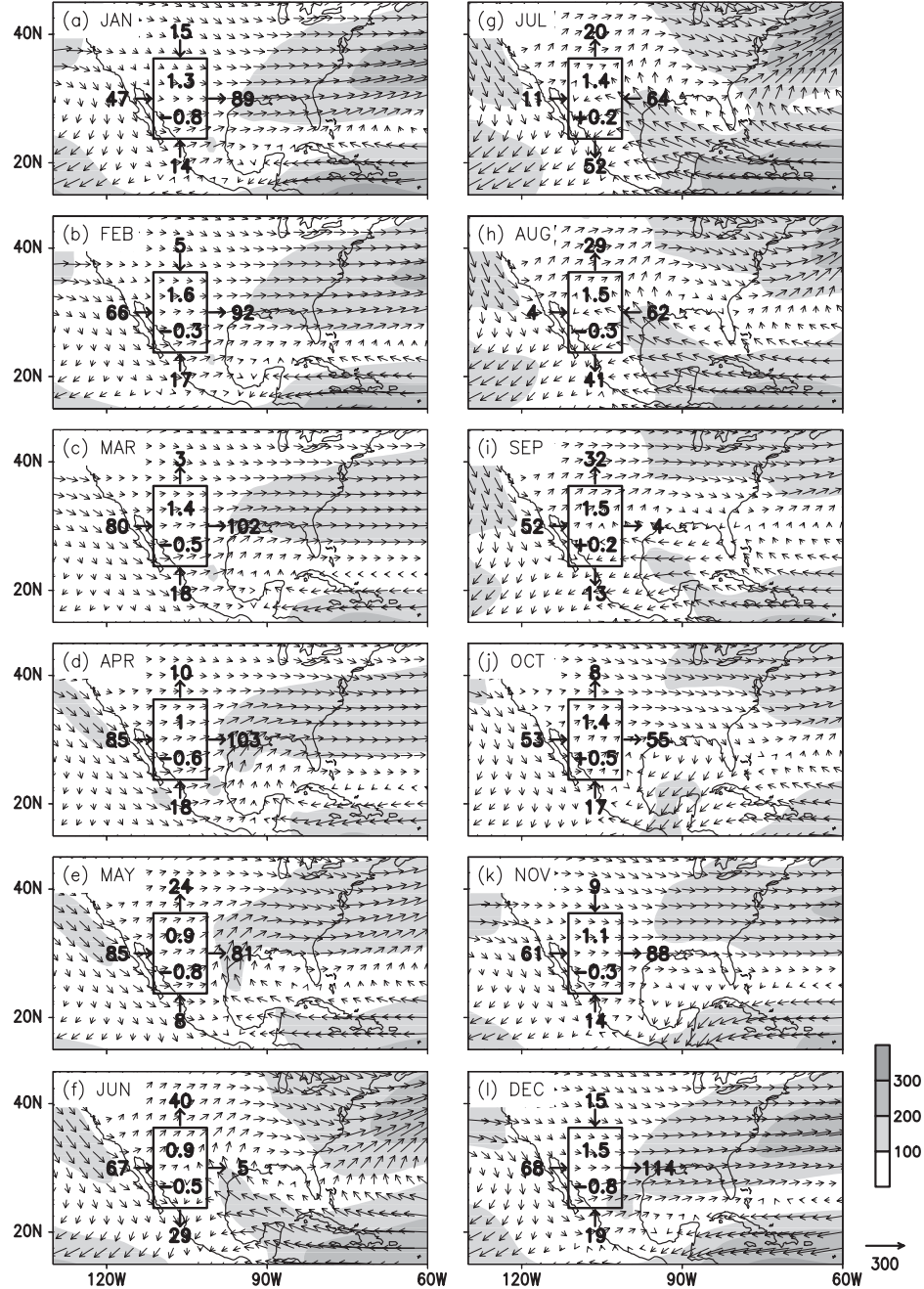


FIG. 12. As in Fig. 11 but for the CFS T62.

and the loss or small gain of water vapor in summer, decreases the amplitude of the annual cycles of water vapor budget and precipitation.

Figure 13 summarizes the main features shown in Figs. 11–12. Presented in the upper portion of the figure are the water vapor fluxes over the western, eastern, southern, and northern boundaries of the SW domain and in the lower portion of the figure are the net water vapor flux and domain-averaged precipitation. The fig-

ure indicates the general consistency between precipitation and net water vapor flux for both observations and the CFS (except in August and December), and the problems of the model discussed above (for Figs. 11 and 12). It also clearly indicates that the problem of the CFS in simulating the summertime moisture budget, and probably precipitation, results mainly from the unrealistic simulation of water vapor flux over the southern boundary.

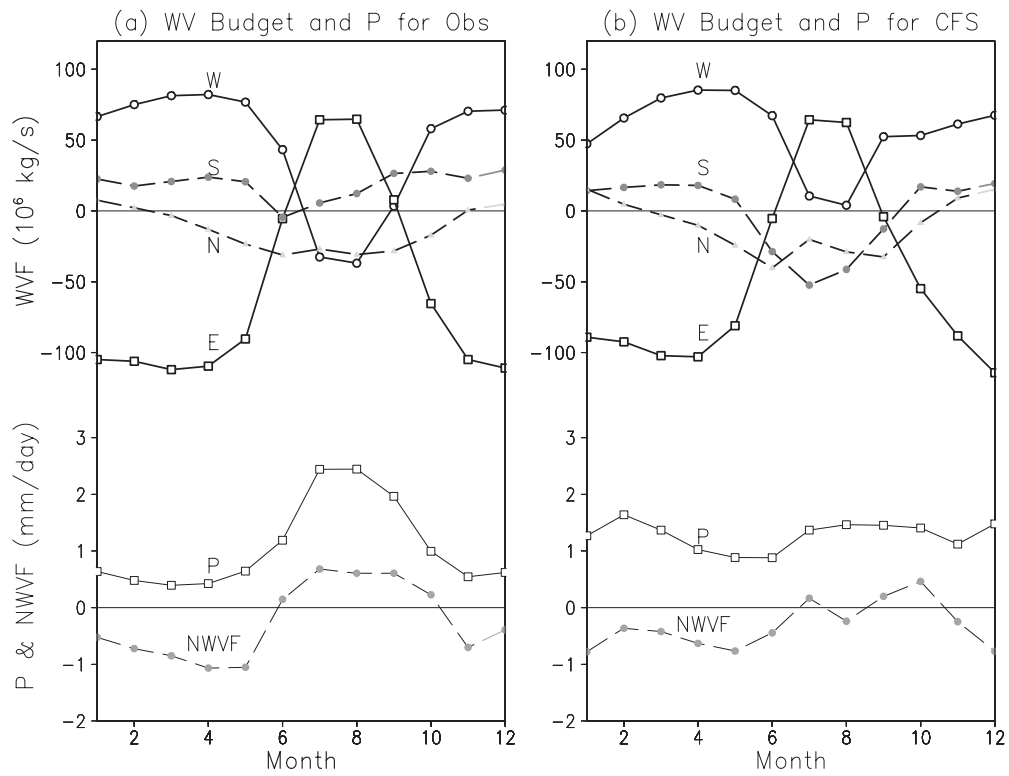


FIG. 13. Water vapor fluxes ( $10^6 \text{ kg s}^{-1}$ ) (a) over the western (W), eastern (E), southern (S), and northern (N) boundaries of the SW domain for observation and (b) for the CFS T62. Positive (negative) values represent the fluxes into (out of) the domain. Shown in the lower portion of the figure are the observed domain-averaged precipitation ( $P$ :  $\text{mm day}^{-1}$ ) and net water vapor flux over SW (NWVF:  $\text{mm day}^{-1}$ ).

The above features shown in water vapor flux are associated with the features in SST and atmospheric circulation patterns. From January to March, the CFS generates a weaker-than-observed anticyclonic pattern over the eastern United States and cooler SST over the western Atlantic (refer to Fig. 4a). The weaker westerlies over the southern United States are linked to less water vapor leaving the SW from the eastern boundary. While this condition continues, errors of southerly wind and warm SST appear over the far eastern Pacific during April–June (refer to Fig. 4b), increasing water vapor flux into the SW from the western boundary. These conditions exaggerate the SW precipitation in the first half of the year in the model. In summer, the CFS simulates a weak low-level jet stream over the Gulf of Mexico, associated with a weak subtropical high and cool SSTs over the Atlantic and the Gulf of Mexico (see Fig. 4c), and water vapor is transported out of the SW domain from its southern boundary. According to Fig. 9b, the warmer-than-observed SST over the tropical eastern Pacific is also associated with decreased precipitation over the Southwest on the semiannual time scale.

This analysis indicates that, while the net water vapor budget in observations is positive in July–September,

the CFS generates either negative or smaller positive net values in these months. It produces smaller (than observed) divergence of water vapor flux in February–May over the Southwest. These features apparently decrease the annual cycle and increase the semiannual signal of net water vapor budget, as seen in the precipitation field. However, in spite of this consistency in the tendency of seasonal changes between water vapor flux and precipitation (for both observations and the CFS), it is noticed that negative water vapor budget appears during all of the nonsummer months (from November to May). Such a deficit in water vapor flux would require constant evaporation from the land surface to maintain the precipitation. Even though precipitation is always light during the nonsummer months, this feature implies a potential problem of the analysis procedure. The potential problem in the imbalance of the moisture budget can be caused by several factors, including data quality and the resolution of the data. The mountains within the analysis domain can also affect the computations of vertical integration and thus the water vapor budget. Difficulties for an accurate estimation of the water vapor budget also come from the unavailability of observed surface evaporation and the

problem with the overly simplified two-layer land surface model in the CFS.

## 5. Summary and discussions

### a. Summary

In this study, we have investigated the variations of U.S. regional precipitation in both observations and free-run experiments with the NCEP CFS. We have analyzed the seasonality of precipitation over the continental United States and the time–frequency characteristics of precipitation over the Southwest. We have also compared the simulations of precipitation between model resolution T62 and a higher resolution of T126, which will be used in the NCEP next-generation CFS.

The most eye-capturing feature of the spatial distribution of U.S. precipitation is the large precipitation over the East and West Coasts, especially over the Gulf Coast and Southeast states, and the small precipitation elsewhere, except over the SW in summer. The precipitation over the SW, northern plains, and the West Coast possesses larger seasonality, and the seasonality of the precipitation over the East (except Florida) and the intermountain area is small. By and large, the CFS simulates the above features reasonably well in many U.S. regions. However, it overestimates the precipitation over the western United States, except the SW in summer, and underestimates the precipitation over the central South, except in spring. It also overestimates the seasonality of precipitation over the intermountain area and Gulf Coast states and underestimates it over the SW, West Coast, and northern Midwest. The model with T126 resolution captures the observed features more realistically than the model with T62 resolution, except for the SW. This improvement of CFS simulations from T62 to T126 is consistent with the result from an analysis of the Asian–Australian and Indo-Pacific monsoon climate (see Yang et al. 2008b).

The variability of observed SW precipitation is characterized by a large annual cycle and a second large semiannual cycle. The oscillating signals on annual, semiannual, and interannual time scales account for 41% of the total precipitation variability. However, the CFS, in both T62 and T126, fails in capturing the above feature. The variability of SW precipitation in the CFS is much less periodic and the oscillating signals on the aforementioned time scales only account for 7% of the total precipitation variability. In particular, the annual oscillation of model precipitation is much weaker than observed and is even much weaker than the simulated semiannual oscillation. The weakly simulated annual cycle is attributed to the unrealistic precipitation simu-

lations of all seasons, especially spring and summer. On the annual time scale, the CFS fails in simulating the relationship between the SW precipitation and the basinwide SST and the overlying atmospheric circulation. On the semiannual time scale, the model exaggerates the response of the regional precipitation to the variations of SST and atmospheric circulation over the tropics and western Atlantic including the Gulf of Mexico. The errors in the simulated semiannual signals distorts the annual cycle in the model. A further analysis indicates that in the simulated SW precipitation a small amplitude bias of the annual signal by  $0.66 \text{ mm day}^{-1}$  and a bias of the phase of the semiannual signal by about 2 months exists. Therefore, enhancing the annual cycle and correcting the error in the phase of the semiannual signal in the CFS are important for improving the simulation of precipitation by the model. In addition, an analysis of the moisture budget over the Southwest shows features consistent with those in precipitation. Particularly for July–September, while water vapor is transported into the Southwest from the southern boundary in the observations, it is moved out of the domain from the boundary in the CFS, largely accounting for the deficit in model precipitation.

### b. Further discussions

To show the robustness of the results obtained, we have compared the features of SW precipitation and those of the precipitation over the NAME tier-1 domain (see Fig. 6a). We have also compared the features between the PREC product and the CPC unified precipitation dataset (Higgins et al. 2000). These analyses of different domains and different datasets have obtained results similar to those presented in the above sections.

Moreover, Kousky (2007) recently analyzed the output from the mode experiment used in this study and from a different experiment that is identical to the one used here but applies different initial conditions. Wen et al. (2008) have also analyzed the statistics of atmospheric quasi-biweekly oscillation over the tropical–subtropical Americas using the same model output (T126) for different segments of 30-yr periods. These studies have shown that the long-term statistics of the CFS output are not sensitive to initial conditions and analysis periods.

This analysis shows that the Southwest is perhaps the only domain over which the simulation of precipitation by the CFS shows little improvement from model resolution T62 to T126. Such a lack of progress indicates a challenge for the forecast system, whose next generation using T126 is expected to become operational in 2010, to predict the North American monsoon. Recently, Long and Schemm (2007) have carried out an

analysis of CFS hindcast simulations and they also indicated that the model encounters substantial difficulties in capturing the observed features of the monsoon in both T62 and T126. However, a T382 version simulates many features of the monsoon more realistically, although the result is based on only one ensemble member.

One of the issues that have not been discussed is the effect of land surface process on the results obtained. As described in section 2, the land surface model currently used in the NCEP CFS is a simple two-layer model (Mahrt and Pan 1984) and it is expected to be replaced by an improved four-layer Noah land surface model (Ek et al. 2003) in the new version of the operational CFS in 2010. Analyses of the output from several experiments have shown noticeable improvements in simulating the precipitation over some U.S. regions from the two-layer land surface model to the four-layer model (R. Yang et al. 2007; L. Long 2008, personal communication). However, no evident progress can be found over the Southwest monsoon domain.

**Acknowledgments.** We are thankful to Viviane Silva, Huug van den Dool, and Hui Wang of the NOAA Climate Prediction Center and three anonymous reviewers, who provided helpful comments for improving the overall quality of the manuscript. Bhaskar Jha provided the AMIP output for computing the Southwest U.S. precipitation used in Fig. 7d. Yundi Jiang and Min Wen were partially supported by the U.S. National Oceanic and Atmospheric Administration and the China Meteorological Administration bilateral program on climate and monsoons.

## REFERENCES

- Behringer, D. W., and Y. Xue, 2004: Evaluation of the global ocean data assimilation at NCEP: The Pacific Ocean. Preprints, *Eighth Symp. on Integrated Observing and Assimilation System for Atmosphere, Ocean, and Land Surface*, Seattle, WA, Amer. Meteor. Soc., 2.3. [Available online at <http://ams.confex.com/ams/pdfpapers/70720.pdf>.]
- Betts, A. K., J. H. Ball, A. C. M. Beljaars, M. J. Miller, and P. A. Viterbo, 1996: The land surface-atmosphere interaction: A review based on observational and global modeling perspectives. *J. Geophys. Res.*, **101**, 7209–7225.
- Boyle, J. S., 1998: Evaluation of the annual cycle of precipitation over the United States in GCMs: AMIP simulations. *J. Climate*, **11**, 1041–1055.
- Chen, M., P. Xie, J. E. Janowiak, and P. A. Arkin, 2002: Global land precipitation: A 50-yr monthly analysis based on gauge observations. *J. Hydrometeor.*, **3**, 249–266.
- Climate Prediction Center, cited 2007: Regional precipitation measurements: December 2007. *Climate Diagnostics Bulletin*. [Available online at <http://www.cpc.ncep.noaa.gov/products/CDB/Extratropics/fige5.shtml>.]
- Dirmeyer, P. A., A. J. Dolman, and N. Sato, 1999: The pilot phase of the global soil wetness project. *Bull. Amer. Meteor. Soc.*, **80**, 851–878.
- Ek, M. B., K. E. Mitchell, Y. Lin, E. Rogers, P. Grunmann, V. Koren, G. Gayno, and J. D. Tarpley, 2003: Implementation of Noah land surface model advances in the National Centers for Environmental Prediction operational mesoscale Eta model. *J. Geophys. Res.*, **108**, 8851, doi:10.1029/2002JD003296.
- FOCRAII, 2006: *Second Session of the Forum on Regional Climate Monitoring, Assessment and Prediction for Asia*. Beijing Climate Center, China Meteorological Administration. [Available online at [http://www.wmo.ch/web/wcp/ccl/topics/FOCRAII-summary\\_1.1.pdf#search=%22FOCRAII%20Summary%22](http://www.wmo.ch/web/wcp/ccl/topics/FOCRAII-summary_1.1.pdf#search=%22FOCRAII%20Summary%22).]
- Gutzler, D. S., and J. W. Preston, 1997: Evidence for a relationship between spring snow cover in North America and summer rainfall in New Mexico. *Geophys. Res. Lett.*, **24**, 2207–2210.
- Harrington, J. A., R. S. Cerveny, and R. Balling, 1992: Impact of the Southern Oscillation on the North American Southwest monsoon. *Phys. Geogr.*, **13**, 318–330.
- Hastenrath, S., 1967: Rainfall distribution and regime in Central America. *Arch. Meteor. Geophys. Bioklimatol.*, **15B**, 201–241.
- Hereford, R., and R. Webb, 1992: Historical variations of warm-season rainfall, southern Colorado Plateau, southwestern U.S.A. *Climatic Change*, **22**, 239–256.
- Higgins, R. W., and W. Shi, 2000: Dominant factors responsible for interannual variability of the summer monsoon in the southwestern United States. *J. Climate*, **13**, 759–776.
- , K. C. Mo, and Y. Yao, 1998: Interannual variability of the U.S. summer precipitation regime with emphasis on the southwest monsoon. *J. Climate*, **11**, 2582–2606.
- , W. Shi, and E. Yarosh, 2000: *Improved United States Precipitation Quality Control System and Analysis*. NCEP/Climate Prediction Center Atlas No. 7, 40 pp.
- , V. B. S. Silva, W. Shi, and V. E. Kousky, 2008: Comparison of daily precipitation statistics for the United States in observations and in the NCEP Climate Forecast System. *J. Climate*, **21**, 5993–6014.
- Hu, Q., and S. Feng, 2002: Interannual rainfall variations in the North American summer monsoon region: 1900–98. *J. Climate*, **15**, 1189–1202.
- Huang, J., and H. M. van den Dool, 1993: Monthly precipitation–temperature relation and temperature prediction over the United States. *J. Climate*, **6**, 1111–1132.
- Kalnay, E., and Coauthors, 1996: The NCEP/NCAR 40-Year Reanalysis Project. *Bull. Amer. Meteor. Soc.*, **77**, 437–471.
- Kanamitsu, M., W. Ebisuzaki, J. Woollen, S.-K. Yang, J. J. Hnilo, M. Fiorino, and G. L. Potter, 2002: NCEP–DOE AMIP-II Reanalysis (R-2). *Bull. Amer. Meteor. Soc.*, **83**, 1631–1643.
- Koster, R. D., and M. J. Suarez, 1995: The relative contributions of land and ocean processes to precipitation variability. *J. Geophys. Res.*, **100**, 13 775–13 790.
- Kousky, V. E., 2007: Comparison of CMIP climatology to CDAS and CAMS-OPI. NOAA Climate Test Bed. [Available online at <http://www.cpc.ncep.noaa.gov/products/ctb/cfs/cfsT126-free-runs.shtml>.]
- Lee, M.-I., and Coauthors, 2007: Sensitivity to horizontal resolution in the AGCM simulations of warm season diurnal cycle of precipitation over the United States and northern Mexico. *J. Climate*, **20**, 1862–1881.
- Li, Q., S. Yang, V. E. Kousky, R. W. Higgins, K. M. Lau, and P. Xie, 2005: Features of cross-Pacific climate shown in the variability of China and U.S. precipitation. *Int. J. Climatol.*, **25**, 1675–1696.

- Liang, J., S. Yang, Z.-Z. Hu, B. Huang, A. Kumar, and Z. Zhang, 2009: Predictable patterns of Asian and Indo-Pacific summer precipitation in the NCEP CFS. *Climate Dyn.*, **32**, 989–1001.
- Long, L., and J. Schemm, 2007: Assessment of the NCEP/CFS on the predictability of the North American monsoon. *Proc. NOAA's 32nd Annual Climate Diagnostics and Prediction Workshop*, Tallahassee, FL, NOAA. [Available online at [http://www.cpc.ncep.noaa.gov/products/outreach/proceedings/cdw32\\_proceedings/](http://www.cpc.ncep.noaa.gov/products/outreach/proceedings/cdw32_proceedings/).]
- Magaña, V., J. A. Amador, and S. Medina, 1999: The midsummer drought over Mexico and Central America. *J. Climate*, **12**, 1577–1588.
- Mahrt, L., and H.-L. Pan, 1984: A two-layer model of soil hydrology. *Bound.-Layer Meteor.*, **29**, 1–20.
- Misra, V., and Y. Zhang, 2007: The fidelity of NCEP CFS seasonal hindcasts over Nordeste. *Mon. Wea. Rev.*, **135**, 618–627.
- Mo, K. C., and J. N. Paegle, 2000: Influence of sea surface temperature anomalies on the precipitation regimes over the Southwest United States. *J. Climate*, **13**, 3588–3598.
- , J.-K. Schemm, H. M. H. Juang, and R. W. Higgins, 2005: Impact of model resolution on the prediction of summer precipitations over the United States and Mexico. *J. Climate*, **18**, 3910–3927.
- Moorthi, S., H.-L. Pan, and P. Caplan, 2001: Changes to the 2001 NCEP operational MRF/AVN global analysis/forecast system. NWS Technical Procedures Bulletin 484, 14 pp. [Available online at <http://www.nws.noaa.gov/om/tpb/484.htm>.]
- Morlet, J., G. Arehs, I. Fourgeau, and D. Giard, 1982: Wave propagation and sampling theory. *Geophysics*, **47**, 203–221.
- Namias, J., 1983: Some causes of United States drought. *J. Climate Appl. Meteor.*, **22**, 30–39.
- O'Lenic, E. A., D. A. Unger, M. S. Halpert, and K. S. Pelman, 2008: Developments in operational long-range climate prediction at CPC. *Wea. Forecasting*, **23**, 496–515.
- Pacanowski, R. C., and S. M. Griffies, 1999: MOM 3.0 manual. NOAA/GFDL, 680 pp.
- Powell, M. J. D., and J. K. Reid, 1969: On applying Householder transformations to linear least squares problems. *Proc. IFIP Congress 1968*, Edinburgh, United Kingdom, IFIP, 122–126.
- Ropelewski, C. F., and M. S. Halpert, 1986: North American precipitation and temperature patterns associated with the El Niño/Southern Oscillation (ENSO). *Mon. Wea. Rev.*, **114**, 2352–2362.
- Saha, S., and Coauthors, 2006: The NCEP Climate Forecast System. *J. Climate*, **19**, 3483–3517.
- Smith, T. M., and R. W. Reynolds, 2003: Extended reconstruction of global sea surface temperatures based on COADS data (1854–1997). *J. Climate*, **16**, 1495–1510.
- Thiaw, W. M., and K.-C. Mo, 2005: Impact of sea surface temperature and soil moisture on seasonal rainfall prediction over the Sahel. *J. Climate*, **18**, 5330–5343.
- Ting, M., and H. Wang, 1997: Summertime U.S. precipitation variability and its relation to Pacific sea surface temperature. *J. Climate*, **10**, 1853–1873.
- Trenberth, K. E., G. W. Branstator, and P. A. Arkin, 1988: Origins of the 1988 North American drought. *Science*, **242**, 1640–1645.
- Walsh, P. D., and N. D. Lawler, 1981: Rainfall seasonality: Description, spatial patterns and change through time. *Weather*, **36**, 201–208.
- Wang, B., and Coauthors, 2008: How accurately do coupled climate models predict the Asian-Australian monsoon interannual variability? *Climate Dyn.*, **30**, 605–619.
- Wang, H., and M. Ting, 2000: Covariabilities of winter U.S. precipitation and Pacific sea surface temperatures. *J. Climate*, **13**, 3711–3719.
- Wang, W., S. Saha, H.-L. Pan, S. Nadiga, and G. White, 2005: Simulation of ENSO in the new NCEP Coupled Forecast System Model. *Mon. Wea. Rev.*, **133**, 1574–1593.
- Wen, M., S. Yang, R. W. Higgins, and R. Zhang, 2008: Summer quasi-biweekly oscillation over the tropical Americas: Spatial features and relation with ENSO. *Proc. NOAA's 32nd Annual Climate Diagnostics and Prediction Workshop*, Tallahassee, FL, NOAA. [Available at [http://www.cpc.ncep.noaa.gov/products/outreach/proceedings/cdw32\\_proceedings/poster-sessions.shtml](http://www.cpc.ncep.noaa.gov/products/outreach/proceedings/cdw32_proceedings/poster-sessions.shtml).]
- Xue, Y., F. Zeng, and C. A. Schlosser, 1996: SSIB and its sensitivity to soil properties—A case study using HAPEX-Mobilhy data. *Global Planet. Change*, **13**, 183–194.
- Yang, R., K. E. Mitchell, J. Meng, H. Wei, and G. Gayno, 2007: Summer season predictions with the next NCEP CFS using different land models and different initial land states. *Proc. NOAA's 32nd Annual Climate Diagnostics and Prediction Workshop*, Tallahassee, FL, NOAA. [Available at [http://www.cpc.ncep.noaa.gov/products/outreach/proceedings/cdw32\\_proceedings/](http://www.cpc.ncep.noaa.gov/products/outreach/proceedings/cdw32_proceedings/).]
- Yang, S., X. Ding, D. Zheng, and Q. Li, 2007: Depiction of the variability of Great Plains precipitation and its relationship with the tropical central-eastern Pacific SST. *J. Appl. Meteor. Climatol.*, **46**, 136–153.
- , M. Wen, and R. W. Higgins, 2008a: Sub-seasonal features of the Asian summer monsoon in the NCEP Climate Forecast System. *Acta Oceanol. Sin.*, **27**, 88–103.
- , Z. Zhang, V. E. Kousky, R. W. Higgins, S.-H. Yoo, J. Liang, and Y. Fan, 2008b: Simulations and seasonal prediction of the Asian summer monsoon in the NCEP Climate Forecast System. *J. Climate*, **21**, 3755–3775.
- Zheng, D. W., and D. N. Dong, 1986: Realization of narrow band filtering of the polar motion data with Multi-Stage Filter. *Acta Astron. Sin.*, **27**, 368–376.
- , B. F. Chao, Y. H. Zhou, and N. H. Yu, 2000: Improvement of edge effect of the wavelet time-frequency spectrum: Application to the length of day series. *J. Geod.*, **74**, 249–254.